


Microstructure and Corrosion Resistance of Laser Additively Manufactured 316L Stainless Steel

JASON R. TRELEWICZ ^{1,3} GARY P. HALADA,¹
OLIVIA K. DONALDSON,¹ and GUHA MANOGHARAN²

1.—Department of Materials Science and Engineering, Stony Brook University, Stony Brook, NY, USA. 2.—Department of Mechanical and Industrial Engineering, Youngstown State University, Youngstown, OH, USA. 3.—e-mail: jason.trelewicz@stonybrook.edu

Additive manufacturing (AM) of metal alloys to produce complex part designs via powder bed fusion methods such as laser melting promises to be a transformative technology for advanced materials processing. However, effective implementation of AM processes requires a clear understanding of the processing–structure–properties–performance relationships in fabricated components. In this study, we report on the formation of micro and nanoscale structures in 316L stainless steel samples printed by laser AM and their implications for general corrosion resistance. A variety of techniques including x-ray diffraction, optical, scanning and transmission electron microscopy, x-ray fluorescence, and energy dispersive x-ray spectroscopy were employed to characterize the microstructure and chemistry of the laser additively manufactured 316L stainless steel, which are compared with wrought 316L coupons via electrochemical polarization. Apparent segregation of Mo has been found to contribute to a loss of passivity and an increased anodic current density. While porosity will also likely impact the environmental performance (e.g., facilitating crevice corrosion) of AM alloys, this work demonstrates the critical influence of microstructure and heterogeneous solute distributions on the corrosion resistance of laser additively manufactured 316L stainless steel.

INTRODUCTION

The evolution of additive manufacturing (AM) to include metal printing has opened up a myriad of new opportunities for the development of new products and for fostering innovation in advanced manufacturing.¹ The principle of AM employs a bottom-to-top approach of rapidly sintering/melting powders layer-by-layer using power sources such as lasers or electron beams to build parts without the need for extensive plastic forming or machining. Optimization of this process has focused extensively on the production of fully dense parts, which depends in large part on the powder chemistry and laser–particle interactions.² The techniques for printing materials layer-by-layer vary from using lasers for selectively solidifying photo-curable polymers to electron-beam processing for selectively melting superalloys.³

There are several approaches for categorizing AM methods based on the nature of raw material,⁴ aggregation geometry during deposition,⁵ and energy or process source.⁶ Alternatively, AM techniques can be categorized based on functional framework such as material, patterning energy, phenomena of creating primitive geometry, nature of adding materials, and support mechanism.⁷ Based on the classification scheme by Williams et al.,⁷ a framework is summarized in Table I that includes electron beam melting (EBM[®]), direct metal laser sintering (DMLS[™]), inverse laser sintering, and laser engineered net shaping (LENS[®]). This study specifically focuses on the powder bed fusion category of AM. As defined by ASTM F2792-12a, powder bed fusion is “an additive manufacturing process in which thermal energy selectively fuses regions of a powder bed”, and commercial examples of this technique include DMLS[™] from EOS and EBM[®] from Arcam.

Table 1. Functional classification of thermal energy-based AM methods adopted from Ref. 7

Process	Store material	Pattern material	Pattern energy	Create primitive	Provide new material	Support material
Electron beam melting (EBM [®])	Single phase powder	No material patterning	1D heat energy	Solidify melt	Recoat by spreading	Bed of build material
Direct metal laser sintering (DMLS TM)	Coated powder Single phase powder	1D powder deposition		Fusion Solidify melt	Direct material addition	5 axis deposition
Inverse laser sintering						
Laser engineered net shaping (LENS [®])						

In the case of powder bed fusion AM, an energy source (laser or electron beam) is targeted at a spread layer of powder material (e.g., metal) to selectively melt segments of this material based on information from each layer of a drawing file. There are several powder bed fusion-laser (PBF-L) processes including DMLSTM and selective laser melting (SLMTM) that fully melt the powder in an inert environment. Several studies have highlighted the relationship between laser processing conditions and the resulting microstructure and, subsequently, mechanical properties. For instance, it was observed that higher heat inputs result in intermetallic phase precipitation in the case of PBF-L Ti-6Al-4V.⁸ Although it requires longer production times, laser re-melting of PBF-L materials has demonstrated improved microstructure and reduced porosity.⁹ Alternative approaches for producing higher quality microstructures have employed multiple laser scanning patterns with predefined overlaps, which have been applied to 316L stainless steel.¹⁰

Applications requiring resistance to pitting and crevice corrosion often use 316L stainless steel with the following alloy chemistry:¹¹ <0.03% C, 16–18.5% Cr, 10–14% Ni, 2–3% Mo, <2% Mn, <1% Si, <0.045% P, < 0.03% S, and balance Fe. A lower carbon content is particularly advantageous for welding processes to inhibit carbide precipitation at grain boundaries. As a result, 316L is widely employed in marine engineering, potable water systems, food preparation equipment, pharmaceutical manufacturing, and medical implants. The latter application has grown immensely in recent years, and 316L can now be found in cardiovascular implants (stents, artificial valves), orthopedic bone fixation devices, orthodontic wires, plates and screws used in craniofacial applications, and artificial eardrums.¹² The corrosion resistance of 316L stainless steel is critical to ensuring biocompatibility since corrosion would not only impact the structural stability of the device but might also result in the release of Ni, which in turn has been found to cause severe inflammation in tissues.¹³

The presence of Mo as an alloying element has a strong impact on the corrosion resistance of austenitic stainless steels. Prior work by the authors has shown that Mo leads to the formation of corrosion inhibiting oxyanions (i.e. molybdate) in the passive film formed on these steels.¹⁴ In addition, it forms an ultrathin Mo-Ni intermetallic layer beneath the passive film,¹⁵ which further protects the base metal and also prevents the ingress of anions such as Cl⁻. Hence, any redistribution of Mo in printed 316L alloys could significantly affect their corrosion resistance.

Grain size also influences the corrosion properties of stainless steels by altering local degradation mechanisms, which have a strong dependence on the corrosive media. For example, studies have demonstrated that decreasing grain size in

austenitic-type 304 stainless steel, particularly below 2 μm , increased the general corrosion rate when subjected to a sulfuric acid solution due to passive film destabilization at grain boundaries.¹⁶ Similarly, low-carbon stainless steels containing nanocrystalline grains at the surface formed via ultrasonic shot peening exhibited enhanced corrosion rates especially at grain sizes below 50 nm.¹⁷ While this finding was attributed to an increase in the number of active sites for corrosion, it is often difficult to decouple grain size from surface chemistry effects. Nevertheless, other studies have also substantiated the complete loss of passivity in 316 stainless steel containing nanocrystalline surface grains.¹⁸

In this paper, 316L stainless steel samples were fabricated using PBF-L AM techniques. The microstructure and corrosion resistance were investigated, and compared to wrought 316L coupons of nominally identical composition. The PBF-L 316L alloys exhibited non-equilibrium heterogeneous microstructural features with segregated Mo that produced a cellular surface structure upon etching. Collectively, Mo segregation and non-equilibrium microstructures containing a range of interfaces and defects led to reduced passivity and an increased anodic current density in a 0.1-M HCl solution.

MATERIALS AND EXPERIMENTAL METHODS

The additively manufactured samples investigated in this study were printed from 316L-8 powder (<0.03% carbon by mass from Renishaw) via PBF-L processing using a Renishaw AM 250 system. A layer thickness of 50 μm was employed with a laser power of 200 W and raster speed of 590 mm/s. Additional process parameters included the focus offset for volume sections set to 0 mm, point distance of 50 μm , and exposure time of 90 μs . Cylindrical rods were produced with a nominal diameter of 25 mm, and subsequently sectioned into 5-mm disks for microscopy and corrosion measurements. All sections were extracted from regions greater than 5 mm from the build surfaces to avoid sampling chemical or structural inhomogeneities associated with the initial or final layers.

Standard metallographic techniques were employed to polish the 5-mm sections to a mirror-like finish where a 0.25- μm diamond suspension was used in the final step. All polished samples were ultrasonically cleaned in propanol and distilled water to remove any remnant polishing suspension. To reveal the microstructure, polished samples were immersed in Vilella's reagent for 25–35 min following ASTM standard E407 for etchant No. 80. The solution contained 95 mL of ethyl alcohol, 5 mL of hydrochloric acid, and 1 g of picric acid. After removal from the Vilella's reagent, the samples were subjected to a 5-min ultrasonic clean in

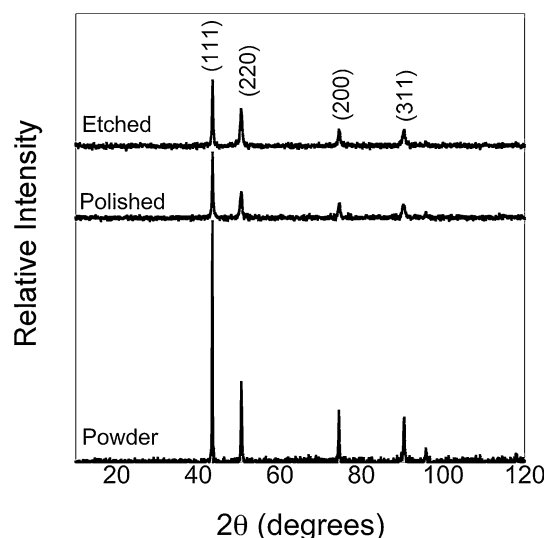


Fig. 1. The XRD spectra for the 316L powder feedstock and PBF-L alloy in polished and etched conditions. All scans revealed the presence of the FCC austenite phase, and subtle peak broadening was apparent in the PBF-L 316L data.

propanol and distilled water. Additional samples of wrought 316L coupons were prepared using the same procedures to provide a baseline response for the corrosion measurements. The wrought alloys were heat-treated in a sealed evacuated quartz tube at 1100°C for 3 h followed by a water quench in order to stabilize the austenitic phase and minimize the sigma phase.

X-ray diffraction (XRD) was performed using the Rigaku Ultima III x-ray diffractometer located in the Center for Functional Nanomaterials (CFN) at Brookhaven National Laboratory (BNL). The Ultima III operates using a copper x-ray cathode tube with a wavelength of 1.54 Å operated at 40 kV and 44 mA. The beam was aligned following placement of the samples on the diffractometer stage using 5° Soller slits. A scan range of 10–120° was selected with a step size of 0.1° and nominal count time of 45 s. Spectral analysis and phase identification was accomplished using the Jade7 software package.

Scanning electron microscopy (SEM) was conducted at Stony Brook University in the Materials Characterization Laboratory using a Leo 1550 Schottky field emission gun SEM. Images were acquired on the etched samples using both backscattered and secondary electron detectors to provide information on surface composition and topography, respectively. An in-lens detector was also employed to provide complimentary high-contrast imaging. Elemental analysis was performed via energy dispersive x-ray spectroscopy (EDS) using an EDAX sapphire detector and IXRF 550i software with particular focus on correlating topographical features with local alloy composition. The average composition of the PBF-L 316L stainless steel was

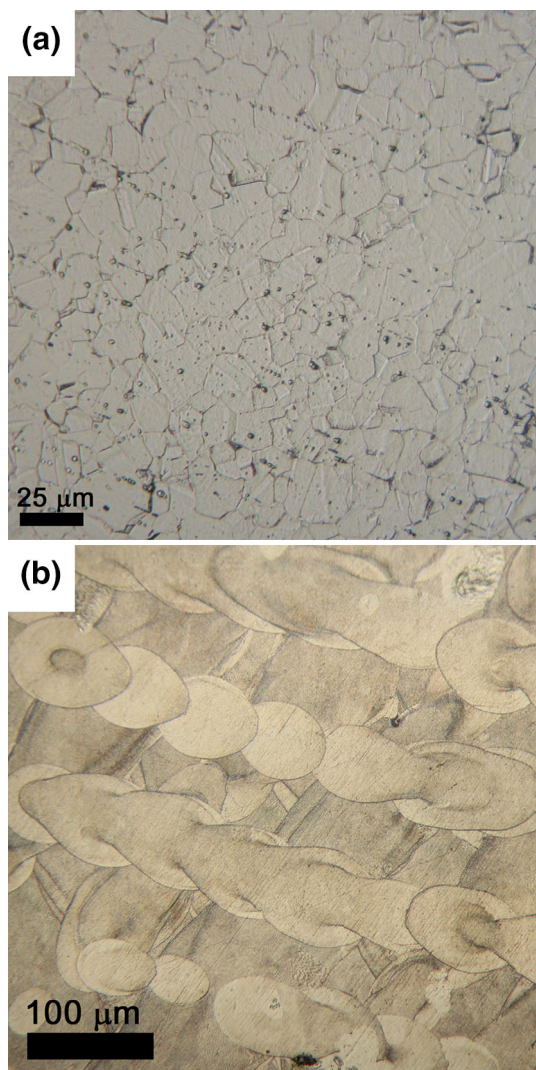


Fig. 2. Optical micrographs of (a) 316L stainless steel sheet following a 30-min etch in Vilella's reagent, and (b) PBF-L 316L stainless steel following a 25-min etch in Vilella's reagent. An equiaxed grain structure was evident in the 316L sheet whereas the PBF-L 316L surface exhibited a heterogeneous structure containing a network of melt pools.

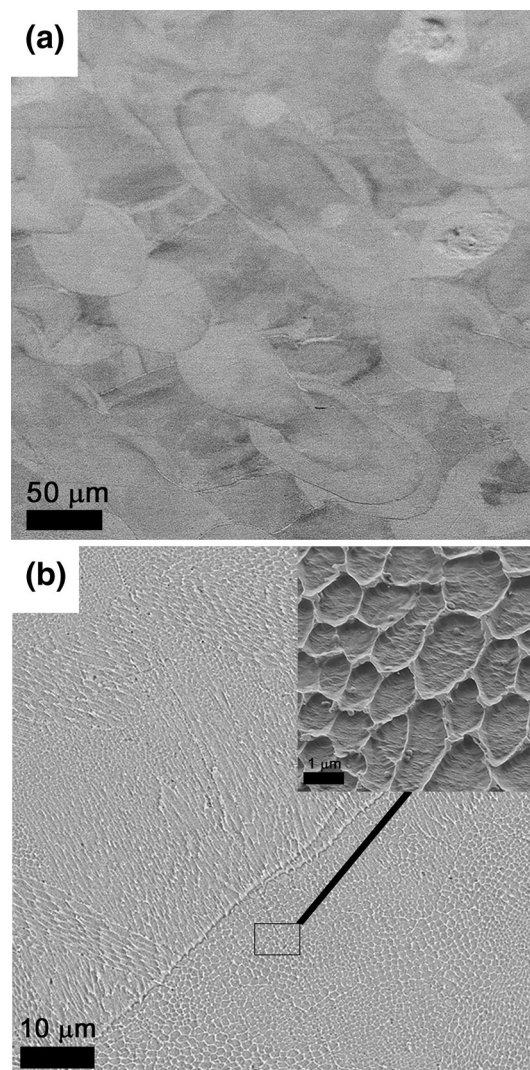


Fig. 3. Secondary electron images of (a) the melt pool structure on the etched surface of PBF-L 316L stainless steel and (b) the cellular structure at the intersection of two misaligned melt pools with a high-magnification view of the denoted region in the inset.

determined via x-ray fluorescence (XRF) using a Niton XL3t Thermoscientific system, and compared with the wrought stainless steel sheet.

Transmission electron microscopy (TEM) was accomplished in the CFN at BNL using a JEOL JEM 2100F field emission TEM operated at 200 kV with the ability for high-resolution imaging. TEM samples were prepared from the polished and etched sections via focused ion beam (FIB) milling in the FEI Helios Nanolab 600 Dual Beam FIB/SEM at CFN. Standard FIB milling techniques employing a platinum sacrificial cap were implemented and coupled with in situ imaging via the SEM capability. The ion-milled samples were attached to an Omniprobe needle and separated from the bulk sample via a U-cut, and subsequently attached to a copper Omniprobe lift-out grid from Ted Pella.

Finally, the sample was removed from the needle and further thinned until reduction in the sacrificial platinum cap was observed. In order to minimize oxidation of the thin sections, all TEM films were stored in a desiccator under vacuum following removal from the FIB.

The FIB TEM samples were placed in either a Gatan single-tilt or double-tilt holder based on the type of tilting required for imaging. Gatan Digital Micrograph software was used for capturing bright and dark field images as well as electron diffraction patterns. Chemical analysis of the sample was performed using an Oxford EDS system equipped with the Inca software package. Quantitative image analysis of the electron diffraction patterns was accomplished using Adobe Photoshop and ImageJ software, where radial intensity profiles were calculated through integration of the intensity over all

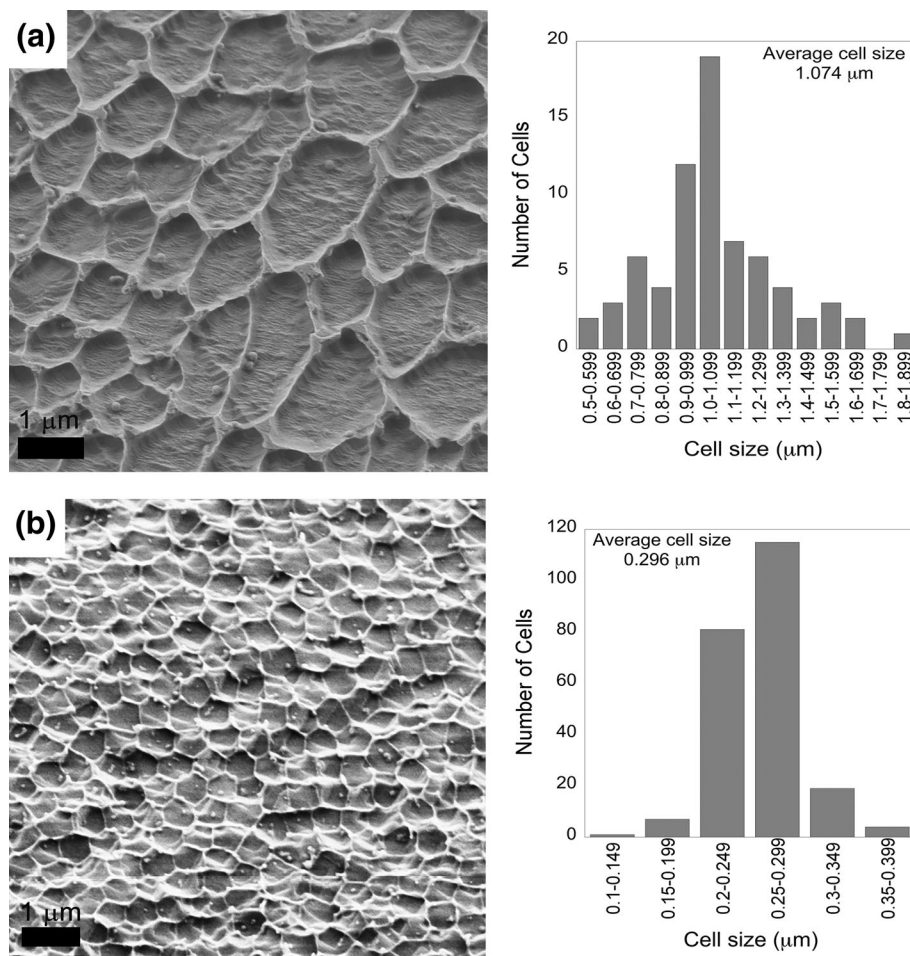


Fig. 4. SEM images of the etched samples with corresponding cell size distributions where the region in (a) exhibited an average size of $1.074 \mu\text{m}$ while the area in (b) an average size of $0.296 \mu\text{m}$.

azimuthal angles as a function of the distance from the center beam.¹⁹ Phases were identified from the integrated intensity profiles using the methods described by Edington,²⁰ where the ratio of the ring spacings were compared to the reciprocal of the d-spacing ratio for possible crystal structures. Results were indexed on the normalized integrated intensity profiles with reciprocal spacings converted to Bragg angles using a wavelength of $\lambda = 0.0273 \text{ \AA}$.

Electrochemical polarization was conducted in a three-electrode glass cell with a platinum wire counter electrode and Ag/AgCl reference electrode. A Gamry Reference 600 potentiostat was employed along with Echem Framework and Echem Analyst software. The cells contained 0.1 M HCl, which was de-aerated for at least 45 min prior to analysis using ultrahigh-purity nitrogen and continually agitated using a magnetic stir-bar during testing. The polish-formed film was reduced by cathodic polarization at -600 mV for 15 min before potentiodynamic scanning.

RESULTS AND DISCUSSION

In this section, results from the materials characterization techniques are presented, and include alloy composition, phase analysis, and microstructure of the PBF-L 316L samples. Local structural data are correlated to mesoscale structure, and collectively used in the discussion of the passivation behavior of PBF-L 316L relative to wrought 316L sheet.

Microstructure and Phase Analysis

Quantitative analysis of the alloying elements in the PBF-L 316L was conducted via XRF and compared with the composition of the wrought sample assessed using the same technique. The composition of the PBF-L 316L, as measured in wt.%, was 64.10% Fe, 17.90% Cr, 12.36% Ni, 2.47% Mo and 1.36% Mn. The 316L sheet exhibited remarkable similarity, containing 64.46% Fe, 17.92% Cr, 12.65% Ni, 2.44% Mo and 1.4% Mn.

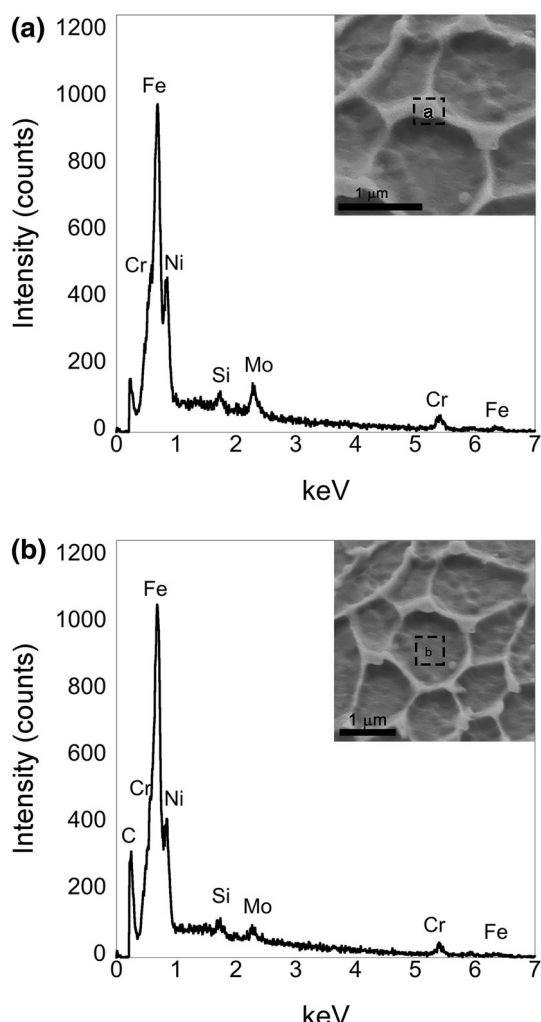


Fig. 5. Elemental analysis from EDS on the (a) cell boundary and (b) cell interior demonstrating the enrichment of Mo at the boundaries, which is accompanied by a reduction in C.

The only two additional elements not quantified by XRF that were identified in EDS measurements were C and Si. Collectively, these elements should only account for less than 2 wt.% of the composition,¹¹ which was thus in good agreement with the balance of the alloys.

The XRD spectra for the PBF-L 316L alloy are shown in Fig. 1 relative to measurements acquired on the feedstock powder. A single sample was first analyzed with the surface polished, followed by measurements on the etched surface to check for the formation of oxides. Indexing of the reflections on the powder sample revealed the presence of the FCC austenite phase, which was retained through PBF-L processing. The broadening and intensity reduction of the peaks in the PBF-L sample was attributed to the refining of the microstructure in the rapidly solidified alloy.^{21,22} However, the peaks were still too sharp to distinguish the size and strain broadening from instrumental broadening, and thus an estimate of crystallite size via the Scherrer,

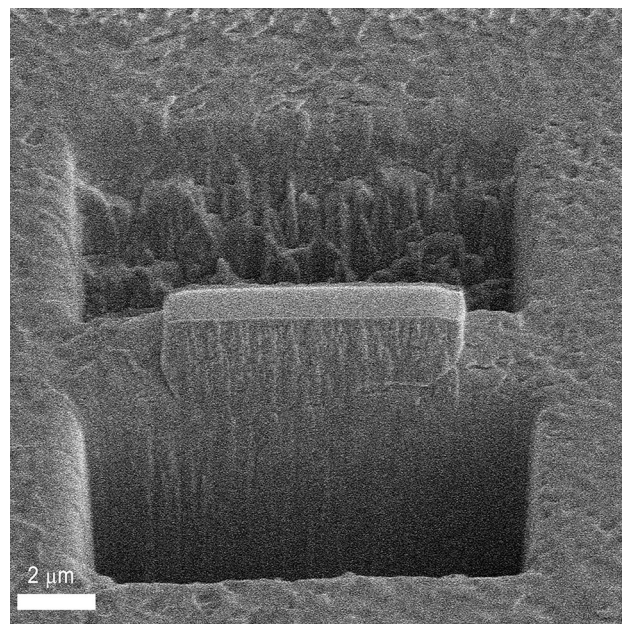


Fig. 6. SEM image of the section milled from the PBF-L 316L alloy using FIB techniques prior to removal from the bulk sample and attachment to the Omniprobe lift-out grid.

Williamson–Hall, or Warren–Averbach methods would not be an accurate representation of grain size.²³ Finally, the spectra for the polished and etched samples were identical, indicating that the etching process did not produce thick surface oxides or other intermetallic phases.

The microstructure of the PBF-L 316L stainless steel was first investigated using optical microscopy on etched surfaces, and was compared with the wrought 316L sheet. The latter exhibited an equiaxed grain structure following a 30-min Vilella etch as evidenced in Fig. 2a, where grain sizes ranged from 10 to 20 μm . Conversely, a 25-min Vilella etch on the PBF-L 316L sample revealed the heterogeneous microstructure depicted in Fig. 2b. A network of melt pools aligned in a weave-like arrangement resulted from the laser-scanning pattern combined with rapid solidification of the locally melted regions. Such accumulative rapid solidification structures are common in PBF-L alloys^{24–27} and lead to considerably different microstructural length scales relative to wrought materials of nominally identical composition.

Higher magnification imaging was performed using SEM, and several important features were uncovered at different magnifications. At low magnification, the aligned melt pools observed in the optical micrographs were evident on the etched surface as shown in Fig. 3a. Increased magnification at the intersection between two adjacent melt pools revealed the cellular structure illustrated in Fig. 3b. This unusual microstructure was a consequence of different etching rates at the cell boundaries relative to the intercellular regions, and has

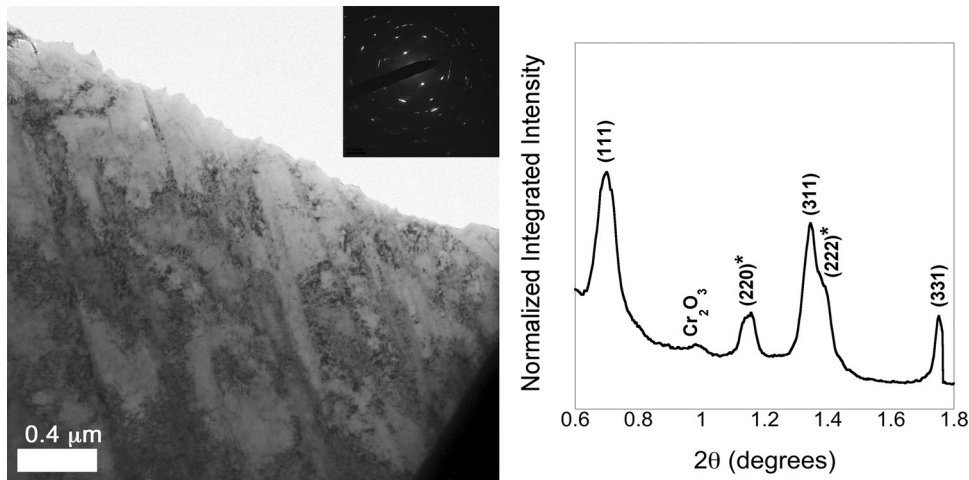


Fig. 7. Bright field image, electron diffraction pattern, and normalized integrated intensity profile for the polished PBF-L 316L sample. A heterogeneous microstructure containing elongated grains was apparent, and the electron diffraction analysis confirmed the presence of FCC austenite. The additional chromium oxide peak was attributed to a thin surface oxide.

recently been observed in a laser additively manufactured 316L part.²⁸ The boundaries between the misaligned melt pools also etched at disparate rates, which delineated the various cell morphologies and aspect ratios that likely resulted from directional heat flow during solidification.

The characteristic cell size within the melt pools varied significantly over the sample surface, as evident in the cell size distributions shown in Fig. 4. The average cell size from the region in Fig. 4a was 1.074 μm while the region in Fig. 4b exhibited a considerably reduced mean cell size of 296 nm. In addition to this wide range of microstructural length scales, non-uniform etch rates produced a ridge-like pattern within the cells, which suggests that underlying structural features also exist at the nanoscale.

Elemental analysis performed via EDS on the heterogeneous PBF-L 316L microstructure focused on distinguishing the composition of the cell boundaries from the interior of the cells, and the results are summarized in Fig. 5. Enrichment of Mo was observed at the cell boundaries as evidenced by the more than 50% increase in the intensity of the Mo $L\alpha$ peak relative to measurements acquired in the cell interior. A slight increase in the Ni $L\alpha$ peak and reduction in the C $K\alpha$ peak accompanied this enhancement of Mo in the intercellular regions. Elemental segregation, as noted below, has significant impact on the corrosion characteristics, and can also lead to the formation of Mo-rich or carbide phases during PBF-L processing.

Connection of the cellular surface structure revealed by etching to the underlying microstructure was accomplished using TEM. An electron-transparent section was extracted from the PBF-L 316L sample using FIB milling, and is shown prior to lift-out in Fig. 6. A region with multiple cells along the

length of the section was selected from an etched sample, and is apparent in the lift-out image. An additional FIB section was prepared from a polished and unetched sample. Collectively, these TEM sections enabled characterization of the underlying microstructural features of the PBF-L 316L alloy.

The bright field TEM image shown in Fig. 7 was acquired on the section removed from the polished PBF-L 316L sample. The microstructure consisted of elongated grains with length scales comparable to the previously described cell sizes, thus suggesting that Mo could in fact be segregating to grain boundaries. However, other defect structures and possible subgrain boundaries were also apparent in the bright field images, which made it difficult to convincingly outline the grain structure in the PBF-L sample. The electron diffraction pattern was indexed to produce the normalized integrated intensity spectrum depicted in Fig. 7. The peaks corresponded to FCC austenite reflections, and were in good agreement with the XRD analysis. The small peak corresponding to chromium oxide was attributed to the formation of a thin surface oxide commonly found on FIB-prepared TEM samples.

The spots corresponding to the (220) and (222) reflections in the electron diffraction pattern were used to produce the dark field images shown in Fig. 8; these peaks are denoted above by asterisks (*). Only the areas corresponding to Bragg reflection for the given orientations are illuminated. Elongated grains were more clearly visible in the dark field images and appeared to contain other defects such as dislocation debris and sub-boundaries. These boundaries roughly corresponded to the spacing of the ridges within the cell interiors in Fig. 4a. Additional measurements are needed to better align the sample with given Bragg reflecting areas for characterization of the underlying defect structure.

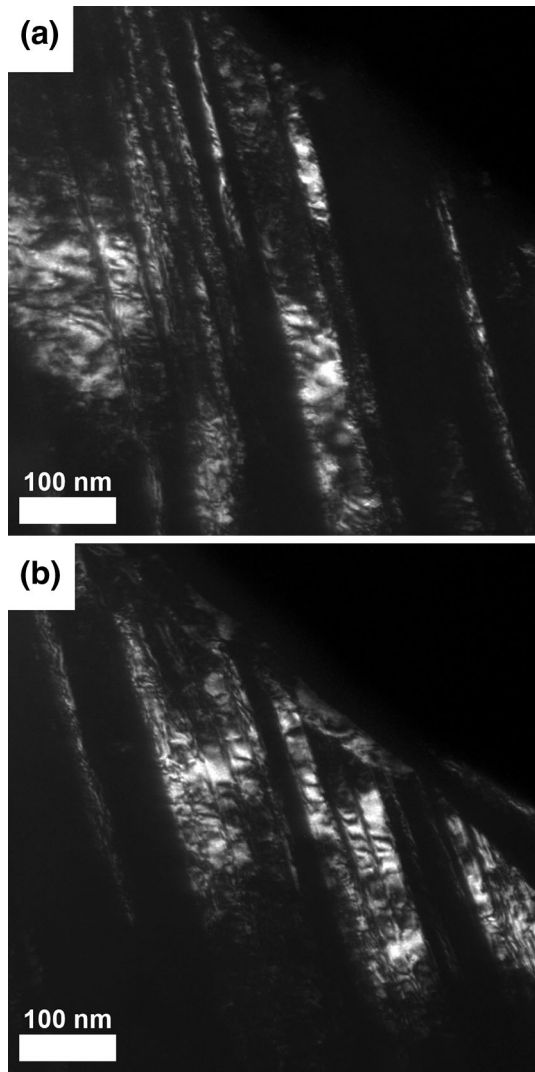


Fig. 8. Dark field images of the polished PBF-L 316L sample highlighting the (a) (220) and (b) (222) orientations of austenite identified in the integrated intensity profile in Fig. 7 by asterisks.

Nevertheless, the bright and dark field images presented here reveal the non-equilibrium nature of the microstructure that results from PBF-L processing of 316L stainless steel.

For comparison with the polished PBF-L 316L sample, the bright field image and electron diffraction analysis from the etched sample are shown in Fig. 9. While it is difficult to discern grain contrast in the bright field image, electron diffraction analysis confirmed the presence of the FCC austenite phase. The identified oxide peak, although different from the Cr_2O_3 phase in the polished sample, was present as a surface film formed on the thin TEM sample. Because this section was extracted from the etched sample containing the cellular surface topography, the cell boundaries or more appropriately walls were evident in the bright field image as sharp protrusions on the surface within the Pt cap. These walls appeared to align with the grain boundaries, although they could also coincide with some other characteristic length scale perhaps pertaining to the distribution of Mo. Future studies will employ scanning transmission electron microscopy (STEM) to discern the relationship between the cellular walls revealed through etching and the underlying solute distribution.

Corrosion and Passivity

As noted above, some degree of microsegregation of Mo occurred during PBF-L processing. This phenomenon has been shown to occur in laser-welded stainless steels, and often degrades the corrosion resistance of the alloy.²⁹ Although this effect has not been widely reported, it somewhat conflicts with other literature that demonstrated enhanced corrosion resistance following laser surface treatments.³⁰ However, in this study, the materials were fully melted and rapidly solidified

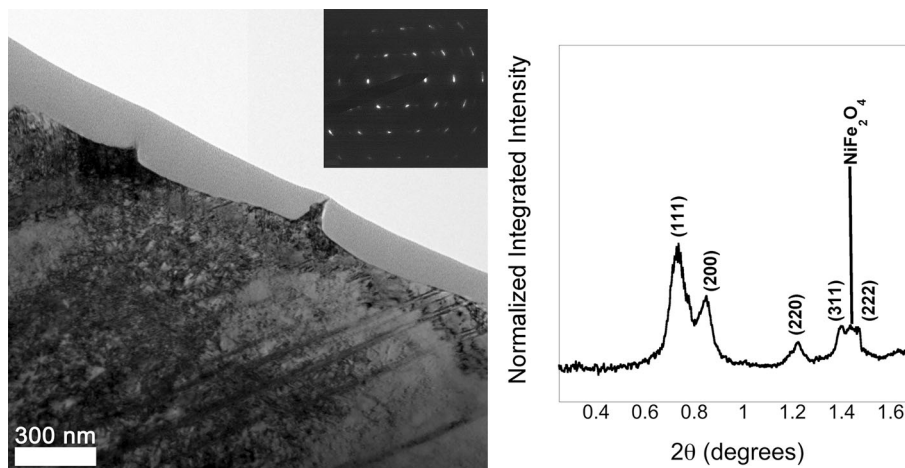


Fig. 9. Bright field and electron diffraction analysis of the etched PBF-L 316L sample. The light gray surface film corresponds to the platinum cap used in the FIB milling technique.

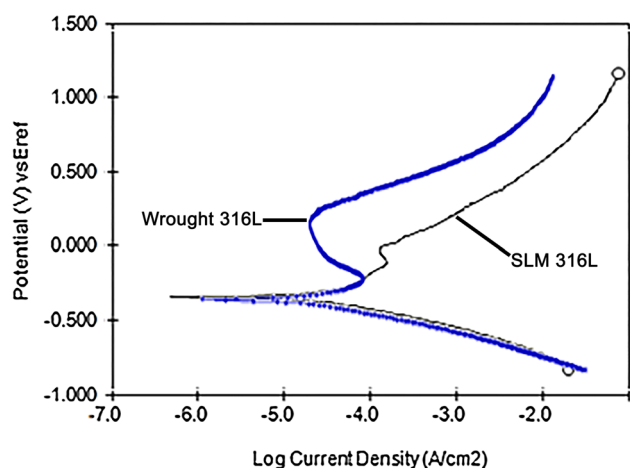


Fig. 10. Potentiodynamic scans performed at 1 mV/s in deaerated 0.1 M HCl versus a Ag/AgCl reference. The trends from the wrought and PBF-L 316L samples are identified accordingly, where the latter exhibited reduced passivity and an increased anodic current density.

during PBF-L processing, which is more akin to the laser welding process with comparable implications for the corrosion resistance.

The potentiodynamic scans collected in deaerated 0.1 M HCl are shown in Fig. 10 for both the wrought and PBF-L 316L samples. The results demonstrated a considerably diminished passive range and an increased passive current density for the printed alloy, which are collectively indicative of a reduced corrosion resistance. The divergence in the passive current density ($22.5 \mu\text{A}/\text{cm}^2$ for wrought 316L versus $135 \mu\text{A}/\text{cm}^2$ for PBF-L 316L) is not likely due to porosity alone, which is substantiated by Kamath et al.³¹ where the density of laser additively manufactured 316L stainless steel produced using similar process conditions approached 99.5% the density of wrought 316L. Furthermore, a complementary study on Inconel 625 demonstrated only a doubling of the passive current density with up to 12% porosity.³² Collectively, these observations suggest that the dramatic increase in the passive current density of PBF-L 316L can be instead attributed to spatially heterogeneous compositional changes caused by elemental segregation. In 316L, Mo is essential to the formation of a passive film, and thus its heterogeneous distribution in the PBF-L alloy can substantially alter passivation mechanisms. Localized attack on weak regions of the passive film likely produced the shift in electrochemical polarization behavior and, in turn, degraded the corrosion resistance of the PBF-L alloy relative to wrought 316L sheet.

The impact of sinter-formed structures on the corrosion resistance of 304L and 316L alloys has also been studied on materials sintered through more traditional heat-treatment techniques.³³ Exposure to a ferric chloride solution demonstrated enhanced corrosion rates relative to cast alloys of

nominally identical compositions. Crevice corrosion mechanisms that were uncovered related to porosity in sintered steels and/or abrasion between adjacent particles, both of which can produce damage to the passive layer. Another recent study investigating the effect of crevice corrosion on 316L stainless steel in 3.5% NaCl reported an altered anodic current density for the crevice sample over a rather large range.³⁴ In light of these findings, while porosity may have contributed to the reduced corrosion resistance of the PBF-L 316L sample, the dominant mechanism likely pertained to the combined effects of inhomogeneous solute distribution and non-equilibrium microstructures on the quality of the passive film.

CONCLUSION

In this work, bulk 316L alloys were synthesized through PBF-L processing, and the resulting materials exhibited a range of non-equilibrium heterogeneous microstructural features. A mesoscale-patterned structure was observed in optical and SEM micrographs that resulted from laser scanning and rapid solidification of the laser melt pools. Within these pools, a network of microscale cells with Mo-enriched etch-resistant intercellular walls were uncovered through etching. At the nanoscale, elongated grains and other defect structures were evident in the TEM micrographs that appeared to coincide with the intercellular Mo-rich walls of the cellular surface structure. The PBF-L 316L alloy exhibited reduced passivity and an increased anodic current density in 0.1 M HCl relative to wrought 316L sheet. This reduced corrosion resistance was attributed to the inhomogeneous solute distribution and non-equilibrium microstructures formed during PBF-L processing. While composition and microstructural variables are proposed to transcend the effect of porosity, future work will focus on confirming these mechanisms through a systematic study of microstructural development, porosity, and passivity as a function of processing parameters and heat treatments in PBF-L 316L stainless steel.

ACKNOWLEDGEMENTS

The authors would like to acknowledge support from the National Center for Defense Manufacturing and Machining (NCDMM)/America Makes and the SUNY Network of Excellence for Materials and Advanced Manufacturing. J.T. and O.D. acknowledge support for this work from the National Science Foundation under Award No. CMMI-1401662. This research used resources of the Center for Functional Nanomaterials, which is a U.S. DOE Office of Science Facility, at Brookhaven National Laboratory under Contract No. DE-SC0012704. J.T. and O.D. would also like to thank Kim Kisslinger at the CFN for his assistance in preparing the FIB TEM samples.

REFERENCES

1. W.E. Frazier, *J. Mater. Eng. Perform.* 23, 1917 (2014).
2. D.D. Gu, W. Meiners, K. Wissenbach, and R. Poprawe, *Int. Mater. Rev.* 57, 133 (2012).
3. G.N. Levy, R. Schindel, and J.P. Kruth, *CIRP Ann.* 52, 589 (2003).
4. D.T. Pham and R.S. Gault, *Int. J. Mach. Tools Manuf.* 38, 1257 (1998).
5. J. Pegna, *Autom. Constr.* 5, 427 (1997).
6. J.P. Kruth, M.C. Leu, and T. Nakagawa, *Progress in Additive Manufacturing and Rapid Prototyping* (Bern: Hallwag Publishers, 1998).
7. C.B. Williams, F. Mistree, and D.W. Rosen, *J. Mech. Des.* 133, 11 (2011).
8. L. Thijs, F. Verhaeghe, T. Craeghs, J.V. Humbeeck, and J.-P. Kruth, *Acta Mater.* 58, 3303 (2010).
9. E. Yasa and J.P. Kruth, *Proc. Eng.* 19, 389 (2011).
10. W. Di, Y. Yongqiang, S. Xubin, and C. Yonghua, *Int. J. Adv. Manuf. Technol.* 58, 1189 (2012).
11. S.D. Washko and G. Aggen, *ASM Handbook: Wrought Stainless Steels, Properties and Selection: Irons, Steels, and High-Performance Alloys* (Ohio: ASM International, 1990).
12. H. Hermawan, D. Ramdan, and J.R. Djuansjah, *Metals for Biomedical Applications* (INTECH Open Access Publisher, 2011).
13. J.C. Wataha, N.L. O'Dell, B.B. Singh, M. Ghazi, G.M. Whitford, and P.E. Lockwood, *J. Biomed. Mater. Res.* 58, 537 (2001).
14. C.R. Clayton, G.P. Halada, and J.R. Kearns, *Mater. Sci. Eng. A* 198, 135 (1995).
15. G.P. Halada and C.R. Clayton, *J. Vac. Sci. Technol. A* 11, 2342 (1993).
16. A. Di Schino and J.M. Kenny, *J. Mater. Sci. Lett.* 21, 1631 (2002).
17. Y. Li, F. Wang, and G. Liu, *Corrosion* 60, 891 (2004).
18. Y.-W. Hao, B. Deng, C. Zhong, Y.-M. Jiang, and J. Li, *J. Iron. Steel Res. Int.* 16, 68 (2009).
19. A.J. Detor and C.A. Schuh, *J. Mater. Res.* 22, 15 (2007).
20. J. Edington, *Practical Electron Microscopy in Materials Science* (New York: Van Nostrand Reinhold Company, 1976).
21. T. Ungár, *Scr. Mater.* 51, 777 (2004).
22. M. Kerber, M. Zehetbauer, E. Schafner, F. Spieckermann, S. Bernstorff, and T. Ungar, *JOM* 63, 61 (2011).
23. Z. Zhang, F. Zhou, and E.J. Lavernia, *Metall. Mater. Trans. A* 34A, 6 (2003).
24. Y.S. Hedberg, B. Qian, Z. Shen, S. Virtanen, and I. Odnevall Wallinder, *Dent. Mater.* 30, 525 (2014).
25. X. Zhou, K. Li, D. Zhang, X. Liu, J. Ma, W. Liu, and Z. Shen, *J. Alloys Compd.* 631, 153 (2015).
26. J.P. Kruth, L. Froyen, J. Van Vaerenbergh, P. Mercelis, M. Rombouts, and B. Lauwers, *J. Mater. Process. Technol.* 149, 616 (2004).
27. J.P. Kruth, M.C. Leu, and T. Nakagawa, *CIRP Ann.* 47, 525 (1998).
28. M. Marya, V. Singh, S. Marya, and J. Hascoet, *Metall. Mater. Trans. B* 46, 1654 (2015).
29. C.T. Kwok, S.L. Fong, F.T. Cheng, and H.C. Man, *J. Mater. Process. Technol.* 176, 168 (2006).
30. C. Carboni, P. Peyre, G. Béranger, and C. Lemaitre, *J. Mater. Sci.* 37, 3715 (2002).
31. C. Kamath, B. El-dasher, G. Gallegos, W. King, and A. Sisto, *Int. J. Adv. Manuf. Technol.* 74, 65 (2014).
32. N. Ahmed, M.S. Bakare, D.G. McCartney, and K.T. Voisey, *Surf. Coat. Technol.* 204, 2294 (2010).
33. E. Otero, A. Pardo, M.V. Utrilla, E. Saenz, and F.J. Perez, *Mater. Charact.* 35, 145 (1995).
34. Z. Wang, Y. Cong, T. Zhang, Y. Shao, and G. Meng, *Int. J. Electrochem. Sci.* 6, 5521 (2011).